



Contents lists available at ScienceDirect

# Journal of Rock Mechanics and Geotechnical Engineering

journal homepage: [www.rockgeotech.org](http://www.rockgeotech.org)

Full Length Article

## Geomechanical analysis of the influence of CO<sub>2</sub> injection location on fault stability

Victor Vilarrasa<sup>a,b,c,\*</sup>, Roman Makhnenko<sup>a,d</sup>, Sohrab Gheibi<sup>e</sup><sup>a</sup> École Polytechnique Fédérale de Lausanne, Lausanne, Switzerland<sup>b</sup> Institute of Environmental Assessment and Water Research (IDAEA-CSIC), Barcelona, Spain<sup>c</sup> Associated Unit: Hydrogeology Group (UPC-CSIC), Barcelona, Spain<sup>d</sup> Department of Civil & Environmental Engineering, University of Illinois at Urbana-Champaign, USA<sup>e</sup> Norwegian University of Science and Technology, Trondheim, Norway

### ARTICLE INFO

#### Article history:

Received 22 March 2016

Received in revised form

29 May 2016

Accepted 6 June 2016

Available online 20 September 2016

#### Keywords:

Carbon dioxide (CO<sub>2</sub>) injection

Geomechanics

Fault stability

Induced seismicity

Fault permeability

### ABSTRACT

Large amounts of carbon dioxide (CO<sub>2</sub>) should be injected in deep saline formations to mitigate climate change, implying geomechanical challenges that require further understanding. Pressure build-up induced by CO<sub>2</sub> injection will decrease the effective stresses and may affect fault stability. Geomechanical effects of overpressure induced by CO<sub>2</sub> injection either in the hanging wall or in the foot wall on fault stability are investigated. CO<sub>2</sub> injection in the presence of a low-permeable fault induces pressurization of the storage formation between the injection well and the fault. The low permeability of the fault hinders fluid flow across it and leads to smaller overpressure on the other side of the fault. This variability in the fluid pressure distribution gives rise to differential total stress changes around the fault that reduce its stability. Despite a significant pressure build-up induced by the fault, caprock stability around the injection well is not compromised and thus, CO<sub>2</sub> leakage across the caprock is unlikely to happen. The decrease in fault stability is similar regardless of the side of the fault where CO<sub>2</sub> is injected. Simulation results show that fault core permeability has a significant effect on fault stability, becoming less affected for high-permeable faults. An appropriate pressure management will allow storing large quantities of CO<sub>2</sub> without inducing fault reactivation.

© 2016 Institute of Rock and Soil Mechanics, Chinese Academy of Sciences. Production and hosting by Elsevier B.V. This is an open access article under the CC BY-NC-ND license (<http://creativecommons.org/licenses/by-nc-nd/4.0/>).

### 1. Introduction

Carbon dioxide (CO<sub>2</sub>) emissions to the atmosphere should be significantly reduced to mitigate climate change. This imperative necessity has recently reached an international consensus at the COP21 meeting in Paris in December 2015. The objective is to limit the temperature increase caused by anthropogenic CO<sub>2</sub> emissions in 2 °C. To achieve this objective, CO<sub>2</sub> emissions should drop by a factor of 2 by 2050 with respect to the current emissions (Fuss et al., 2014). According to the International Energy Agency (IEA), geologic carbon storage has the potential to contribute to one fifth of the total CO<sub>2</sub> emissions reduction (IEA, 2010). This percentage represents storing 8 Gt/yr of CO<sub>2</sub> in deep geologic formations by 2050. This huge amount of CO<sub>2</sub> would be injected in multiple industrial-

scale projects that would capture CO<sub>2</sub> from industrial point sources, implying a continuous mass flow rate in the order of millions of tons per year in each injection well during several decades (Szulczewski et al., 2012).

Maintaining CO<sub>2</sub> injection over years will cause the pressurization of large areas within the storage formation (Birkholzer et al., 2015). Even though the radius of the CO<sub>2</sub> plume may be of a few kilometers, the radius of the pressure perturbation cone with an overpressure higher than 0.1 MPa can exceed hundreds of kilometers for an injection of several decades (Birkholzer et al., 2009). Higher pressure cutoffs that may induce fault stability issues in critically stressed faults, such as 1 MPa, can extend tens of kilometers (Birkholzer et al., 2009; Verdon, 2014). Furthermore, once large-scale geologic carbon storage projects will be fully deployed, superposition of overpressure from different injection wells in the same sedimentary basin is expectable, leading to an even larger pressurized region (Zhou and Birkholzer, 2011). Thus, in spite of the fact that injection wells will most likely be placed far away from identified faults to minimize the risk of fault reactivation,

\* Corresponding author.

E-mail address: [victor.vilarrasa@upc.edu](mailto:victor.vilarrasa@upc.edu) (V. Vilarrasa).

Peer review under responsibility of Institute of Rock and Soil Mechanics, Chinese Academy of Sciences.

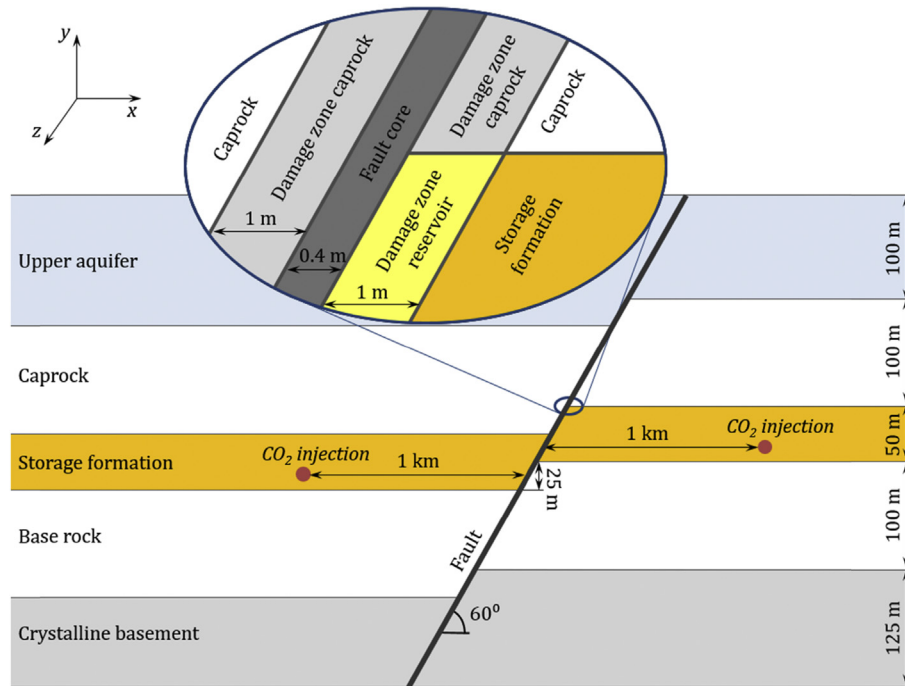


**Fig. 1.** Schematic representation of the model geometry. CO<sub>2</sub> is injected either in the hanging wall or in the foot wall 1 km away from the fault, which has an offset of 25 m. The fault is composed of a fault core, which extends all along the fault, and damage zones on both sides of the core. The damage zones vary for each rock type, as indicated in the inset.

overpressure will eventually reach faults in the far field, affecting their stability (Streit and Hillis, 2004).

Fault stability analysis associated with CO<sub>2</sub> injection is usually modeled in reservoirs of limited size (Vidal-Gilbert et al., 2010). CO<sub>2</sub> injection in closed storage formations bounded by low-permeable faults may lead to fault reactivation if no pressure management is performed (Cappa and Rutqvist, 2011a; Mazzoldi et al., 2012). One concern related to fault reactivation is the potential of shear slip to open up migration paths through which CO<sub>2</sub> could leak (Zoback and Gorelick, 2012). However, CO<sub>2</sub> leakage is unlikely to happen because (1) fault reactivation usually occurs in the crystalline basement, below the storage formation (Verdon, 2014); (2) the caprock sealing capacity is likely to remain unaffected (Pan et al., 2013, 2014; Vilarrasa et al., 2014); and (3) the heterogeneity of faults hinders CO<sub>2</sub> upwards migration (Rinaldi et al., 2014). More importantly, fault reactivation is accompanied by a seismic event. CO<sub>2</sub> injection has the potential to induce seismicity of magnitude three that could be felt on the ground surface (Cappa and Rutqvist, 2012). Felt induced seismic events should be avoided because they generate nuisances and fear in the local population, which may lead to the closure of geologic carbon storage projects (Oldenburg, 2012). There are already several examples of fluid injection projects that have been halted because of felt induced seismicity, like the geothermal project at Basel in Switzerland (Häring et al., 2008), the seasonal natural gas storage project of Castor in Spain (Cesca et al., 2014), and wastewater disposal wells at Guy-Greenbrier, Arkansas (Horton, 2012) and Youngstown, Ohio in the USA (Ellsworth, 2013).

The studies that model fault reactivation induced by CO<sub>2</sub> injection usually consider injection in the hanging wall of the fault (Cappa and Rutqvist, 2011b; Rinaldi et al., 2015), though, in fact, it may occur on either side of the fault (Pereira et al., 2014). Furthermore, these studies have focused on predicting the magnitude of the induced earthquakes resulting from the fault slip caused during fault reactivation, but not on the changes in effective stresses induced by overpressure and stress redistribution that occur around the fault and that trigger fault instability.

The aim of this paper is to investigate how CO<sub>2</sub> injection, either in the hanging wall or in the foot wall, affects fault stability. We first present the geometry of the considered problem, justify the material properties for each rock and explain the numerical solution to the problem. Then, we show the numerical results for fault stability when injecting CO<sub>2</sub> in the hanging wall and in the foot wall of an extensional fault. Finally, we discuss the implications of this study and draw the conclusions.

## 2. Methods

### 2.1. Geometry

We model the lower portion of a sedimentary basin (Fig. 1). The main feature of the model is a normal fault with an inclination of 60°. This fault becomes critically oriented in a normal faulting stress regime, like the one of the model, if its friction angle equals 30° (Vilarrasa et al., 2013a). The fault is formed by a fault core and damage zones on both sides of the core (Caine et al., 1996). The fault core is assumed to have the same properties all along the fault. However, the damage zones have different properties depending on the rock types that they are in contact with. We distinguish three types of damage zones: one for clastic rocks typical of reservoirs, one for shaly materials that act as confinement layers, and another one for the crystalline basement.

Plane strain conditions are assumed due to the geometry of the problem, which is extensive in the out-of-plane direction. CO<sub>2</sub> is injected through a horizontal well either in the hanging wall (left of the fault in Fig. 1) or in the foot wall (right of the fault in Fig. 1) in a 50 m-thick storage formation. The injection wells are placed 1 km away from the fault. The offset of the fault is 25 m, so half of the storage formation overlaps on both sides of the fault. The storage formation is overlaid and underlain by low-permeable and high entry pressure formations. The confinement layers have a thickness of 100 m. Below the base rock, the model includes the upper 100 m and 125 m of the crystalline basement on the hanging wall and the

foot wall of the fault, respectively. Above the caprock, a secondary aquifer is modeled. The thickness of this aquifer is 125 m and 100 m on the hanging wall and the foot wall, respectively. The top of the secondary aquifer is placed at a depth of 1275 m. The geologic medium on the top of the secondary aquifer is not included in the model, but an overburden of equivalent weight is applied on the top of the model. The model extends laterally 15 km on both sides of the fault.

## 2.2. Governing equations

To simulate CO<sub>2</sub> injection in a deep saline aquifer, mass conservation and momentum conservation of both CO<sub>2</sub> and water have to be solved. Mass conservation of these two fluids can be written as (Bear, 1972):

$$\frac{\partial(\varphi S_{\alpha} \rho_{\alpha})}{\partial t} + \nabla \cdot (\rho_{\alpha} \mathbf{q}_{\alpha}) = r_{\alpha} \quad (\alpha = c, w) \quad (1)$$

where  $\varphi$  is the porosity;  $S_{\alpha}$  is the saturation degree of  $\alpha$ -phase;  $\rho_{\alpha}$  is the density of  $\alpha$ -phase;  $t$  is the time;  $\mathbf{q}_{\alpha}$  is the volumetric flux of  $\alpha$ -phase;  $r_{\alpha}$  is the phase change term, i.e. CO<sub>2</sub> dissolution into water and water evaporation into CO<sub>2</sub>; and  $\alpha$  is either the CO<sub>2</sub>-rich phase (c) or the aqueous phase (w). We neglect evaporation of water into CO<sub>2</sub>, i.e.  $r_w = 0$ .

The volumetric flux in Eq. (1) is given by momentum conservation of the fluid phases, which for slow laminar flow in permeable porous media is described by Darcy's law:

$$\mathbf{q}_{\alpha} = -\frac{k k_{r\alpha}}{\mu_{\alpha}} (\nabla p_{\alpha} + \rho_{\alpha} \mathbf{g} \nabla z) \quad (\alpha = c, w) \quad (2)$$

where  $k$  is the intrinsic permeability,  $k_{r\alpha}$  is the relative permeability of  $\alpha$ -phase,  $\mu_{\alpha}$  is the viscosity of  $\alpha$ -phase,  $p_{\alpha}$  is the pressure of  $\alpha$ -phase,  $\mathbf{g}$  is the gravity acceleration, and  $z$  is the vertical coordinate.

The overpressure resulting from CO<sub>2</sub> injection will induce deformation and modify the stress state in the geologic media. The momentum balance of the solid phase needs to be solved to take into account the mechanical effects, and if inertial terms are neglected, the momentum balance reduces to the equilibrium of stresses:

$$\nabla \cdot \boldsymbol{\sigma} + \mathbf{b} = \mathbf{0} \quad (3)$$

where  $\boldsymbol{\sigma}$  is the stress tensor with  $\sigma_x$ ,  $\sigma_y$ , and  $\sigma_z$  being the diagonal elements and  $\tau_{xy}$ ,  $\tau_{yz}$ , and  $\tau_{zx}$  being the off-diagonal elements; and  $\mathbf{b}$  is the body forces vector.

We assume that the geologic media remain elastic throughout the whole simulation and that the stress–strain relationship is given by the generalized Hooke's law:

$$\boldsymbol{\varepsilon} = \frac{\sigma'_m}{3K} \mathbf{I} + \frac{1}{2G} (\boldsymbol{\sigma}' - \sigma'_m \mathbf{I}) \quad (4)$$

where  $\boldsymbol{\varepsilon}$  is the elastic strain tensor;  $\mathbf{I}$  is the identity matrix;  $\boldsymbol{\sigma}'$  is the effective stress tensor defined as  $\boldsymbol{\sigma}' = \boldsymbol{\sigma} - p \mathbf{I}$ , where  $p$  is the maximum between water and CO<sub>2</sub> pressures;  $\sigma'_m = \text{tr}(\boldsymbol{\sigma}')/3$  is the mean effective stress;  $K = E/[3(1 - 2\nu)]$  is the bulk modulus,  $G = E/[2(1 + \nu)]$  is the shear modulus, where  $E$  is the Young's modulus, and  $\nu$  is the Poisson's ratio. We assume that stress and strain are positive in compression and negative in extension.

To evaluate fracture stability, we conservatively assume that a cohesionless critically oriented fracture could exist at every point, meaning that a standard Mohr–Coulomb failure criterion can be

used. Adopting Mohr–Coulomb failure criterion, the mobilized friction angle can be calculated as

$$\phi_{\text{mob}} = \arctan\left(\frac{\tau}{\sigma'_n}\right) \quad (5)$$

where  $\tau$  is the tangential stress, and  $\sigma'_n$  is the normal effective stress acting on the cohesionless critically oriented fracture. The mobilized friction angle gives an idea of how close the stress state is to failure conditions. The higher the mobilized friction angle, the higher the potential for slip reactivation. If the mobilized friction angle equals the actual friction angle, shear failure conditions are reached and the fracture or fault would undergo shear slip, which could induce seismicity. In general, the actual friction angle of geomaterials can be considered as 30° (Byerlee, 1978).

## 2.3. Material properties

Berea sandstone with permeability of  $\sim 10^{-14}$  m<sup>2</sup> is considered to form the storage formation. Swiss shale – Opalinus clay – is taken as a ductile clay-rich (>55% of clay) low-permeable (with the  $k$  value of  $\sim 10^{-20}$  m<sup>2</sup>) caprock and base rock representative. The upper aquifer consists of Indiana limestone (with the  $k$  value of  $\sim 10^{-14}$  m<sup>2</sup>) and the crystalline basement is formed by Charcoal granite (with the  $k$  value of  $\sim 10^{-20}$  m<sup>2</sup>). The material properties were measured in conventional triaxial experiments and reported at corresponding effective mean stresses (Table 1) (e.g. Makhnenko and Labuz, 2016). Gas entry values and porosities are obtained from mercury intrusion porosimetry tests. The reported values of porosity for the confining layers, crystalline basement, and the fault core are the effective porosities, i.e. those contributing to flow. Relative CO<sub>2</sub> and water permeabilities are taken as power functions of saturation, with a power of 3 for the sandstone and the limestone and 6 for the shale and the granite (Bennion and Bachu, 2008).

Properties of the fault (Table 2) are reported as those of the crushed (remolded) shale and damaged sandstone for the fault core and damage zone reservoirs, respectively. Damage zone confinement layers and damage zone basement properties are those of the damaged shale and granite, respectively.

The elastic parameters for the storage formation, upper aquifer, and damage zone reservoir are taken as those related to the drained (long-term) regime of deformation, because the characteristic diffusion time (Detournay and Cheng, 1993) for these rocks is in the order of 1–10 min. Conversely, the undrained (short-term) elastic parameters are reported for the intact and damaged zone confining layers and intact and damaged crystalline basement due to their characteristic time scale of the diffusion processes, which is in the order of 5–500 years. The characteristic pressure diffusion time across the fault core is about two days, which is two orders of magnitude smaller than the considered injection time (1 year), hence the drained response is assumed.

## 2.4. Numerical solution

We first solve the equilibration of fluid pressure and stresses. Water pressure is hydrostatic and the partial pressure of CO<sub>2</sub> equals 0.01 MPa, which corresponds to an initial concentration of dissolved CO<sub>2</sub> of  $2.44 \times 10^{-5}$  kg/kg of water. We consider that the model is isothermal, with a temperature equal to 60°. This temperature is representative of the temperature of the storage formation (at depth of 1.5 km) assuming a geothermal gradient of 33 °C/km and a surface temperature of 10 °C. The initial stress state corresponds to a normal faulting stress regime, i.e. the vertical

**Table 1**  
Material properties of the rock types included in the model.

Material	Permeability, $k$ (m <sup>2</sup> )	Relative water permeability, $k_{rw}$	Relative CO <sub>2</sub> permeability, $k_{rc}$	Gas entry pressure, $p_0$ (MPa)	Van Genuchten shape parameter, $m$	Porosity	Young's modulus, $E$ (GPa)	Poisson's ratio, $\nu$
Storage formation	$4 \times 10^{-14}$	$S_w^3$	$S_c^3$	0.02	0.8	0.23	14	0.31
Caprock	$8 \times 10^{-20}$	$S_w^6$	$S_c^6$	10	0.3	0.05	2.8	0.4
Base rock	$5 \times 10^{-20}$	$S_w^6$	$S_c^6$	10	0.3	0.05	3	0.39
Upper aquifer	$1 \times 10^{-14}$	$S_w^3$	$S_c^3$	0.2	0.8	0.13	28	0.21
Crystalline basement	$4 \times 10^{-20}$	$S_w^6$	$S_c^6$	12	0.3	0.01	84	0.18

**Table 2**  
Properties of the materials forming the fault.

Material	Permeability, $k$ (m <sup>2</sup> )	Relative water permeability, $k_{rw}$	Relative CO <sub>2</sub> permeability, $k_{rc}$	Gas entry pressure, $p_0$ (MPa)	Van Genuchten shape parameter, $m$	Porosity	Young's modulus, $E$ (GPa)	Poisson's ratio, $\nu$
Fault core	$1 \times 10^{-19}$	$S_w^6$	$S_c^6$	4	0.3	0.1	1	0.3
Damage zone reservoirs	$2 \times 10^{-13}$	$S_w^3$	$S_c^3$	0.02	0.8	0.25	7	0.35
Damage zone confinement layers	$1.5 \times 10^{-19}$	$S_w^6$	$S_c^6$	5	0.3	0.09	1.4	0.42
Damage zone basement	$1 \times 10^{-16}$	$S_w^4$	$S_c^4$	1	0.5	0.07	42	0.3

stress,  $\sigma_v$ , is the maximum principal stress and is given by an average density of the geologic media of 23 MPa/km. The initial horizontal stress is obtained from  $\sigma_h = 0.69\sigma_v$ , which provides a mobilized friction angle of 22.2°, typical of sedimentary basins (Vilarrasa and Carrera, 2015).

CO<sub>2</sub> is injected for 1 year at a rate of  $2 \times 10^{-3}$  kg/s per meter in the direction normal to the model plane in the well placed either in the hanging wall or in the foot wall. The horizontal wells are modeled by a vertical line of 1 m, placed 5 m above the bottom of the storage formation. If the horizontal wells were 2 km in length, a total amount of 4 kg/s would be injected, which represents injecting 0.126 Mt/yr of CO<sub>2</sub>. This injection rate is within the range of those at In Salah, Algeria, where the storage formation has a similar permeability to the one considered in this study (Rutqvist, 2012). We impose constant pressure on the outer boundaries, placed 15 km away from the fault on both sides of the model. No flow is considered at the top and bottom boundaries. The mechanical boundary conditions are a constant stress equal to the weight of the overburden on the top boundary and no displacement perpendicular to the other boundaries.

The two-phase flow problem in deformable porous media is solved in a fully coupled way using the finite element code CODE\_BRIGHT (Olivella et al., 1994, 1996), which has been extended for CO<sub>2</sub> injection (Vilarrasa et al., 2013b). The mesh is made of 5775 quadrilateral elements, with a higher refinement around the fault and the injection wells. Vertically, the elements have a size of 4 m in the storage formation and the lower portion of the caprock, progressively increasing up to 35 m at the top and bottom boundaries. Horizontally, the elements are of tens of centimeters around the fault and of metric scale around the wells, and progressively increase to a size of 2 km at the outer boundaries. The fault core thickness is discretized in two elements and the damage zones on each side of the core in three elements. We have ensured that a further refinement of the mesh does not affect the results.

### 3. Results

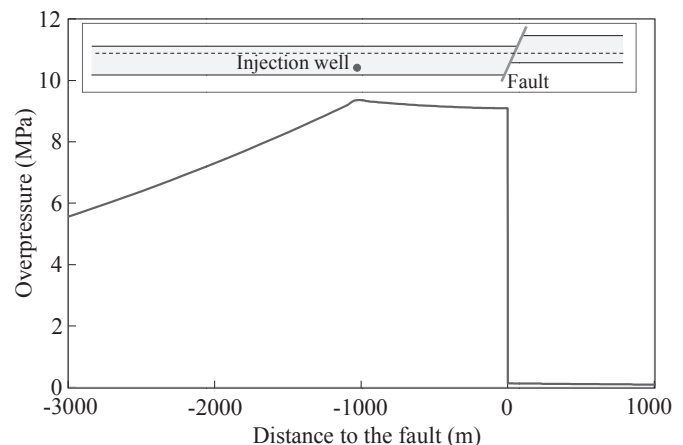
#### 3.1. CO<sub>2</sub> injection in the hanging wall

CO<sub>2</sub> injection in the proximity of a low-permeable fault (1 km in this case) causes the pressurization of the region between the

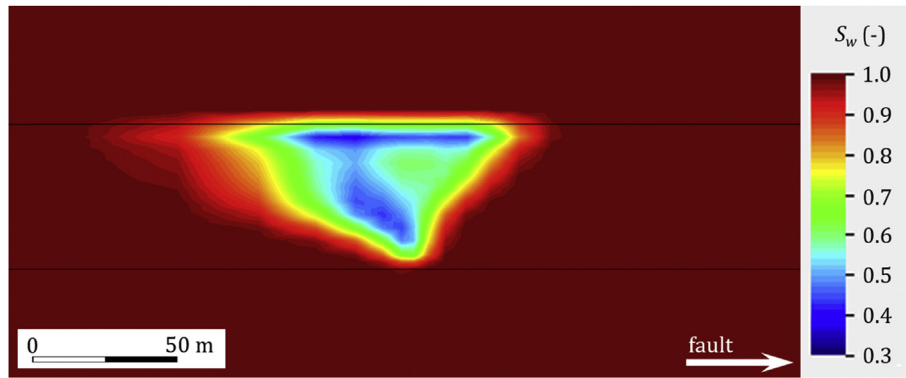
injection well and the fault (Fig. 2). If the fault core is low-permeable, it acts as a flow barrier reducing the flow rate across the fault to a negligible quantity and preventing pressure build-up on the other side of the fault, i.e. the foot wall when CO<sub>2</sub> is injected in the hanging wall (Fig. 2). Unlike the region between the injection well and the fault, overpressure dissipates significantly with distance to the injection well on the side that is open. This pressure distribution has a direct effect on CO<sub>2</sub> dynamics.

Fig. 3 illustrates how the presence of a low-permeable fault affects the shape of the CO<sub>2</sub> plume. Since fluid pressure around the plume is higher on one side of the fault than that on the other side, CO<sub>2</sub> is pushed away from the fault, resulting in an asymmetry of the plume. This CO<sub>2</sub> plume shape can give information on the presence of low-permeable faults that affect the pressure distribution.

Fig. 4 displays the stress changes (Fig. 4b–e) caused by the overpressure (Fig. 4a) and the induced changes in rock stability (Fig. 4f). The horizontal total stress increases proportionally to overpressure in the out-of-plane direction, i.e. parallel to the fault (Fig. 4d). Thus, the horizontal total stress increases in the hanging wall of the fault, but not in the foot wall. In the direction



**Fig. 2.** Overpressure distribution after one year of CO<sub>2</sub> injection in the hanging wall of a low-permeable fault. Overpressure is measured at a horizontal section that coincides with the middle of the portion of the storage formation that overlaps on both sides of the fault, as indicated by the dashed line in the inset.



**Fig. 3.** CO<sub>2</sub> plume after one year of injection in the hanging wall, 1 km away from the fault. Note that the plume is asymmetric due to the higher overpressure on the side closer to the fault, which pushes the injected CO<sub>2</sub> away from the fault. The side where the fault is located is indicated with an arrow.

perpendicular to the fault, the horizontal total stress change presents a similar distribution to that in the out-of-plane direction, but the presence of the fault alters the total stress changes around it (Fig. 4b). This anomaly in the stress change extends on both sides of the fault for a distance that is approximately equal to the thickness of the storage formation. The region not affected by the presence of the fault has a similar increase in the horizontal total stresses in all directions. This increase is very similar to the analytical estimation that can be done according to the total stress increment induced by overpressure in a laterally extensive aquifer, which equals  $\Delta\sigma_h = \Delta p(1 - 2\nu)/(1 - \nu)$  (Rutqvist, 2012).

Around the fault, the horizontal total stress increases in the direction perpendicular to the fault in the foot wall in the lower half of the storage formation, which overlaps with the upper part of the storage formation in the hanging wall (Fig. 4b). Furthermore, the horizontal total stress increases by a lower magnitude than that in the rest of the hanging wall in the lower portion of the storage formation, which coincides with the base rock on the other side of the fault. These stress changes are due to the fact that overpressure causes an expansion of the storage formation, which compresses the rock around it. Thus, the lower portion of the storage formation in the foot wall of the fault and the upper portion of the caprock below it undergo compression. The storage formation accumulates more stress because it is one order of magnitude stiffer than the confining layers. Interestingly, the base rock causes a lower increase in the horizontal total stress in the direction perpendicular to the fault in the lower half of the storage formation in the hanging wall, presenting a minimum with almost no horizontal total stress increment close to the fault (Fig. 4b).

Stress redistribution around the fault also affects the vertical total stress (Fig. 4c), which increases in the fault core. Additionally, it also increases at the position close to the fault in the upper half of the storage formation in the hanging wall and in the upper part of the caprock in the foot wall. In contrast, the relative increase is small at the position close to the fault in the lower half of the storage formation in the hanging wall and the vertical total stress decreases in the lower half of the storage formation in the foot wall.

The total stress changes in the vertical and horizontal directions lead to a non-trivial shear stress distribution around the fault (Fig. 4e). Below the storage formation, shear stress changes correspond to those typical of a fault in a normal faulting stress regime, with the hanging wall pointing downwards and the foot wall pointing upwards. Above the storage formation, the opposite shear stress changes are induced, with the hanging wall pointing upwards and the foot wall pointing downwards. This is due to the fact that CO<sub>2</sub> injection causes an expansion of the storage formation on the side where it is injected, i.e. the hanging wall in this case. This

expansion pushes the rock upwards above the storage formation and downwards below the storage formation. Additionally, the stress redistribution around the fault induces shear stress changes that point upwards on both sides of the fault in the region where the storage formation overlaps on both sides of the fault (Fig. 4e). In contrast, the shear stress changes point downwards on both sides of the fault in the lower half of the storage formation in the hanging wall and the upper portion of the base rock in the foot wall.

Fig. 4f shows the change in the mobilized friction angle caused by CO<sub>2</sub> injection. While a positive change in the mobilized friction angle means that the rock becomes more unstable because the stress state approaches failure conditions, a negative change leads to a more stable situation. The most critical region is that close to the fault in the lower half of the storage formation in the hanging wall. In contrast, stability improves in the storage formation in the foot wall. Interestingly, the caprock stability experiences a very small change, which suggests that the caprock sealing capacity is not compromised.

Fig. 5 displays the mobilized friction angle around the fault at three horizontal planes. Stability remains unaltered in the plane that crosses the caprock in the hanging wall and the upper portion of the storage formation in the foot wall (green dotted line). In the intermediate plane (blue line), i.e. the one that crosses the fault through the middle of the section in which the storage formation overlaps on both sides of the fault, stability decreases in the hanging wall (the side of the fault where CO<sub>2</sub> is injected) and improves in the foot wall. Stability decreases even more in the lower half of the storage formation in the hanging wall (dashed red line). The least stable conditions occur outside the fault: the most critical zone is placed inside the storage formation around 0.5 m away from the damage zone. On the other side of the fault, stability also decreases in the base rock, but within the first 5 m from the fault, the mobilized friction angle is approximately equal to the initial one.

Fig. 6 depicts the time evolution of the mobilized friction angle at several points. In the zone where the storage formation overlaps on both sides of the fault, the mobilized friction angle increases, meaning that stability decreases in the damage zone of the hanging wall (point A), but slightly decreases (stability improves) in the damage zone of the foot wall (point B). The stability increase in the foot wall (point B) is caused by a decrease in the vertical total stress (Fig. 4c) and an increase in the horizontal total stress (Fig. 4b) combined with an almost constant fluid pressure. The resulting effective stresses lead to shrinkage of the Mohr circle (Fig. 7), thus stability improves. On the other hand, point A undergoes a similar change in the total stress in horizontal and vertical directions, which leads to a shift of the Mohr circle towards the failure envelope due to the build-up in fluid pressure occurring in the hanging wall (Fig. 7).

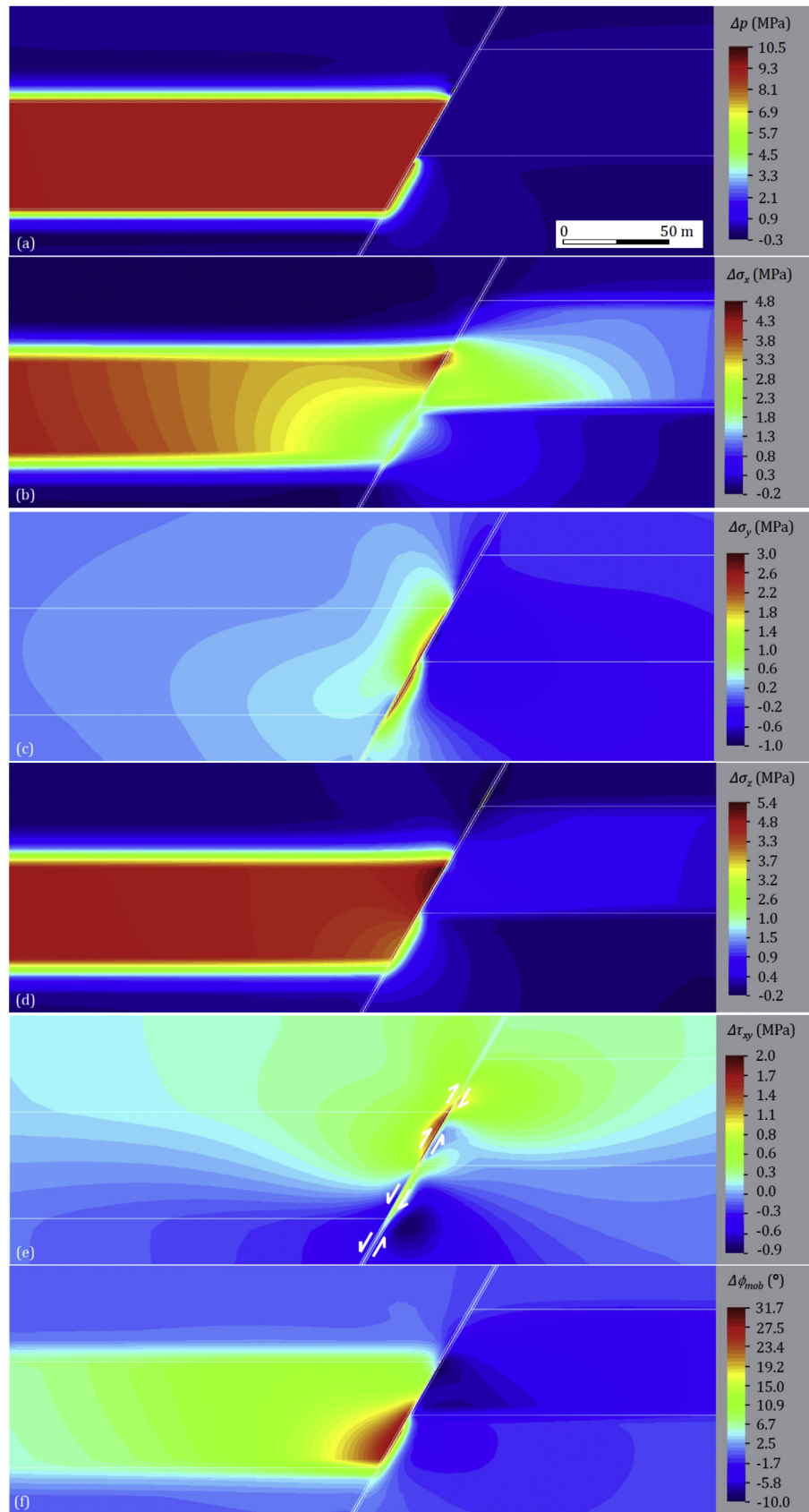


**Fig. 4.** Distribution of changes in (a) fluid pressure, (b) minimum horizontal total stress (in-plane), (c) vertical total stress, (d) maximum horizontal total stress (out-of-plane), (e) shear stress, and (f) mobilized friction angle after one year of injecting CO<sub>2</sub> in the hanging wall.

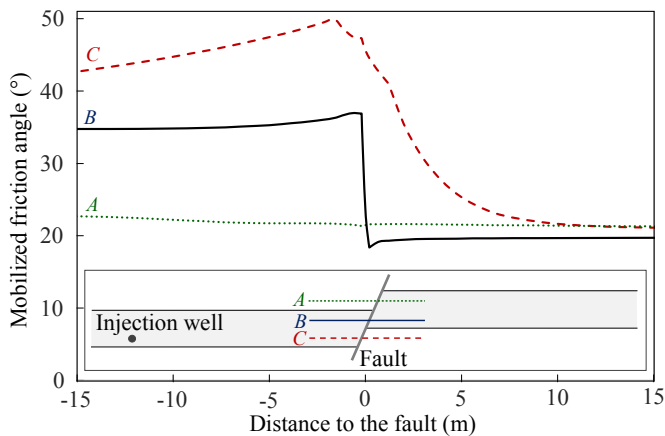


Fig. 5. Mobilized friction angle at three sections crossing the fault (see inset) after one year of injecting CO<sub>2</sub> in the hanging wall.

In the lower half of the storage formation in the hanging wall, the mobilized friction angle increases more rapidly than that in the section where the storage formation overlaps on both sides of the fault (Fig. 6a). This higher rate is caused by the lower increase in the horizontal total stress that occurs in this lower portion of the storage formation, which leads to an increase in the size of the Mohr circle (Fig. 7). The most critical point (point C) is placed around 0.5 m away from the damage zone. Even though a lower increase in the vertical total stress in point C with respect to point D leads to a smaller Mohr circle, the lower horizontal total stress increment leads to a Mohr circle that is closer to the yield surface.

Fig. 6b shows three additional points: a point in the fault core below the storage formation (point E), a point in the upper portion of the storage formation in the foot wall (point F), and a point in the fault core above the storage formation (point G). Two of these points (F and G) present almost no change in the mobilized friction angle. In point E, placed below the storage formation, the mobilized friction angle decreases initially, but it subsequently increases. This trend in the mobilized friction angle follows the same evolution as liquid pressure. Liquid pressure initially drops due to the reverse-water level fluctuation or Noordbergum effect (Hsieh, 1996; Vilarrasa et al., 2013a), but after some time, pressure diffuses through the low-permeable fault core and eventually causes pressure build-up, which is significantly lower than that occurring in the storage formation. The reverse-water level fluctuation is caused by deformation-induced pressure changes occurring in layers that overlay and underlay the formation where fluid is injected.

Fig. 8 displays the mobilized friction angle on a horizontal section that coincides with the middle of the portion of the storage formation that overlaps on both sides of the fault. The dotted line indicates the initial mobilized friction angle. Interestingly, despite the large overpressure induced by the presence of the low-permeable fault, increase in the mobilized friction angle is small around the injection well. Thus, caprock stability is maintained and its sealing capacity is not compromised. However, the mobilized friction angle varies significantly in the vicinity of the fault. Even though stability improves in the foot wall, the high mobilized friction angles in the hanging wall of the fault (higher than typical values of friction angle of geomaterials that are around 30°) suggest that shear failure is likely to occur in the fault.

### 3.2. CO<sub>2</sub> injection in the foot wall

When CO<sub>2</sub> is injected in the foot wall, overpressure and the induced total stress changes are very similar compared with those

in the case of injection in the hanging wall, but occurring on the other side of the fault (Fig. 9). Since the fault has a 25 m-offset, the results are not exactly symmetric, though overpressure and total stress changes, both in vertical and horizontal directions, have similar magnitudes and distributions compared to those in the case of CO<sub>2</sub> injection in the hanging wall. The shear stress change has the same sign as in a normal faulting stress regime above the storage formation because now the rock above the storage formation in the foot wall is pushed upwards (Fig. 9e). Below the storage formation in the foot wall, which is pushed downwards, the shear stress changes have the opposite sign. In the upper half of the storage formation in the foot wall and in the portion of the caprock that is on the opposite side of the fault in the hanging wall, shear stress changes point upwards on both sides of the fault. In contrast, in the section of the storage formation that overlaps on both sides of the fault, shear stress changes point downwards on both sides of the fault.

The most critical region, when CO<sub>2</sub> is injected in the foot wall, takes place in the upper half of the storage formation in the foot wall close to the fault (Fig. 9f). Similarly to CO<sub>2</sub> injection in the hanging wall, stability also improves on the other side of the fault where CO<sub>2</sub> is injected. In this case, the maximum mobilized friction angle is slightly higher than that when CO<sub>2</sub> is injected in the hanging wall.

### 3.3. Effect of fault permeability on fault stability

To evaluate the effect of fault core permeability on fault stability, we also present the results of CO<sub>2</sub> injection in the hanging wall with the core permeability equal to 10<sup>-17</sup> m<sup>2</sup>, i.e. two orders of magnitude higher than that in the previous case, but still three orders of magnitude lower than that of the storage formation. A higher permeability of the fault core has a significant effect on pressure distribution (Fig. 10). First, the injection pressure for a constant mass injection rate becomes smaller than that for the less permeable fault. Second, the pressure gradient in the region between the injection well and the fault becomes higher for a more permeable fault core. This pressure distribution leads to a lower pressure on the fault in the hanging wall. Finally, the liquid flow across the fault core is non-negligible and causes pressure build-up on the foot wall (Fig. 11a).

The liquid pressure increase in the storage formation in the foot wall induces an increase in the horizontal total stresses there (Fig. 11b and d). Similar to the case with a less permeable fault core, the horizontal total stress in the direction perpendicular to the fault has a higher increase at the position close to the fault in the section of the storage formation that overlaps on both sides of the fault than that in the part coinciding with the base rock. Since the overpressure is lower than that in the case with a less permeable fault, the changes in the total stresses are also smaller. In this case, the shear stress changes are small, but present a clear pattern: the pressurized region of the fault, which mainly coincides with the storage formation on both sides of the fault, has a shear stress change that points upwards in the hanging wall and downwards in the foot wall (Fig. 11e). This change in the shear stress is caused by the expansion of the storage formation induced by CO<sub>2</sub> injection in the hanging wall and has opposite sign to the shear stress acting on a fault in a normal faulting stress regime.

Fig. 11f shows that the most critical zone is, like in the case of a fault core with lower permeability, the lower half of the storage formation in the hanging wall close to the fault. However, the increase in the mobilized friction angle is moderate in this case, which suggests that shear failure conditions may not be reached, at least for the time scale of this simulation. In spite of the pressure build-up in the foot wall, the mobilized friction angle decreases in

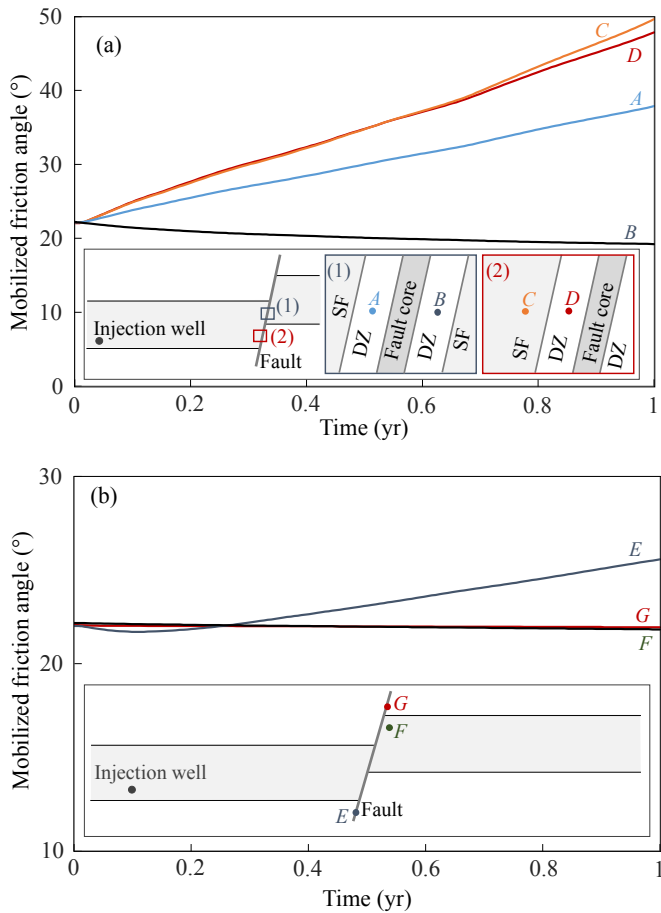


**Fig. 6.** Evolution of the mobilized friction angle at several points when injecting CO<sub>2</sub> in the hanging wall (a) in and close to the fault in the pressurized part of the storage formation and (b) below and above the storage formation and in the upper portion of the storage formation that is not pressurized. SF and DZ stand for storage formation and damage zone, respectively.

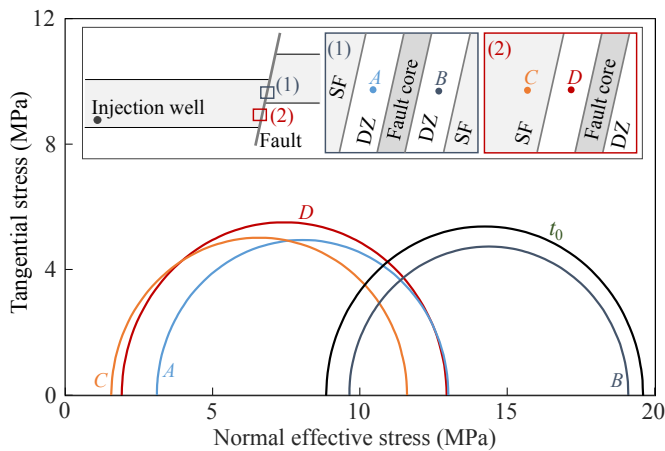


**Fig. 7.** Mohr circles before injection and after one year of injecting CO<sub>2</sub> in the hanging wall at several points. *t*<sub>0</sub> represents the initial stress state.

the section of the storage formation that overlaps on both sides of the fault. This is due to the mechanical effect that causes an increase in the horizontal total stress in the direction perpendicular to the fault in this region (Fig. 11b) that is higher than the decrease in effective stresses induced by overpressure (Fig. 11a). In contrast, the

upper portion of the storage formation in the foot wall close to the fault experiences an increase in the mobilized friction angle. This decrease in stability is a result of the reduction in the effective stresses due to the overpressure and the negligible increase in the horizontal total stress in the direction perpendicular to the fault.

Fig. 12 compares the evolution of the mobilized friction angle resulting from a fault core of relatively high permeability ( $10^{-17} \text{ m}^2$ ) and one with lower permeability ( $10^{-19} \text{ m}^2$ ) at the same points as in Fig. 6. In the most critical zone, i.e. in the lower half of the storage formation in the hanging wall close to the fault (points C and D), the mobilized friction angle increases regardless of the fault core permeability. Nevertheless, the increase rate is higher for the case of a lower fault core permeability because the pressure builds up faster. In the section where the storage formation overlaps on both sides of the fault (points A and B), a more permeable fault core leads to a lower mobilized friction angle increase in the hanging wall (point A), for the same reason as in points C and D. On the other side of the fault, a lower decrease occurs in the foot wall (point B) because of the higher overpressure caused by the higher flow across the more permeable fault. The higher overpressure on the foot wall that occurs in the presence of a relatively permeable fault core leads to an increase in the mobilized friction angle in points F and G, which were not affected in the case with a lower permeability. Finally, in the fault core below the storage formation (point E), a similar trend as in the case of a lower permeability fault core occurs, but with a faster pressure diffusion. The faster pressurization of the fault core limits the reverse-water level fluctuation to a very limited time (a few days) and pore pressure increases rapidly, leading to a faster increase in the mobilized friction angle.

**4. Discussion**

Simulation results show that there are only small differences between injecting in the hanging wall and in the foot wall. The maximum mobilized friction angle is slightly higher when injecting in the foot wall than that in the hanging wall, which suggests that CO<sub>2</sub> injection in the former one is more critical than that in the latter one. Nevertheless, the differences are relatively small, so fault stability can be equally compromised if CO<sub>2</sub> is injected either in the hanging wall or in the foot wall. Therefore, the location of the injection well, either in the hanging wall or in the foot wall, should not be a critical factor in the design of fluid injection projects.

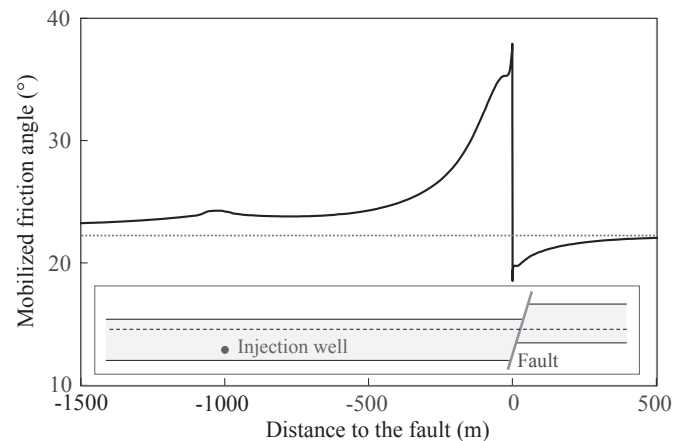


**Fig. 8.** Distribution of the mobilized friction angle after one year of CO<sub>2</sub> injection in the hanging wall, computed at a horizontal section that coincides with the middle portion of the storage formation that overlaps on both sides of the fault, as indicated by the dashed line in the inset.

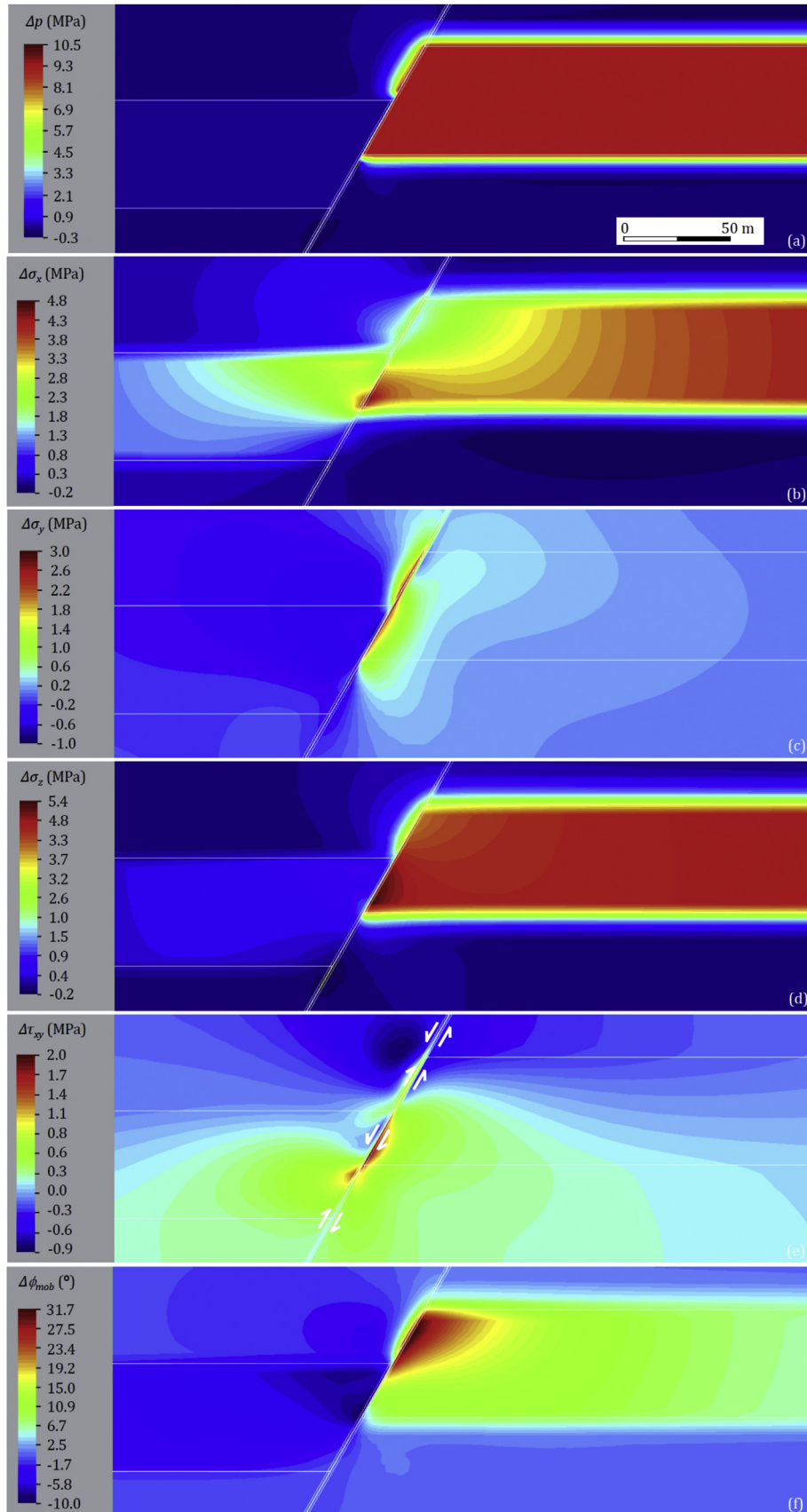


**Fig. 9.** Distribution of changes in (a) fluid pressure, (b) minimum horizontal total stress (in-plane), (c) vertical total stress, (d) maximum horizontal total stress (out-of-plane), (e) shear stress, and (f) mobilized friction angle after one year of injecting CO<sub>2</sub> in the foot wall.

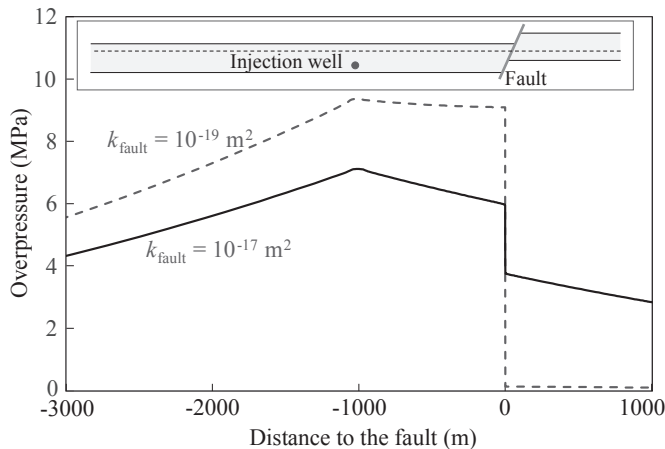


**Fig. 10.** Overpressure distribution after one year of  $\text{CO}_2$  injection in the hanging wall of a fault with a fault core permeability of  $10^{-17} \text{ m}^2$ . For comparison, the induced overpressure for the case of the fault with a core permeability of  $10^{-19} \text{ m}^2$  is shown. Overpressure is measured at the horizontal section coinciding with the middle portion of the storage formation that overlaps on both sides of the fault, as indicated by the dashed line in the inset.

However, identifying faults is crucial because their stability can be seriously affected (Fig. 8).

Faults cannot be avoided in compartmentalized reservoirs (Castelletto et al., 2013). Thus, they can be a limiting factor that can shorten the injection period, as reported in Snøhvit, Norway, where  $\text{CO}_2$  injection had to be stopped after a few months due to an excessive overpressure induced by low-permeable faults (Hansen et al., 2013). As a result, injection wells should be located as far as possible from faults to minimize fault stability issues and avoid posing limitations on the injection rate. Nevertheless, the pressure perturbation cone will advance tens to hundreds of kilometers for the injection time scales expected in geologic carbon storage projects (Birkholzer et al., 2015). Hence, a proper pressure management will be required to minimize the risk of inducing felt seismic events (Vilarrasa and Carrera, 2015).

Unlike fault stability, which decreases as a result of  $\text{CO}_2$  injection, caprock and storage formation stability away from the fault is not compromised (Fig. 8). In particular, the caprock remains stable around the injection well despite the large pressure build-up induced in the storage formation by the low-permeable fault. Hence, the caprock sealing capacity will be maintained and thus, no  $\text{CO}_2$  leakage will occur. The injection rate and overpressure (close to 10 MPa) of our simulation are similar to those at In Salah in Algeria, where no  $\text{CO}_2$  leakage across the caprock has been detected (Rutqvist, 2012). Furthermore,  $\text{CO}_2$  is pushed away from the fault due to the higher overpressure between the fault and the injection well compared to the other side of the injection well where no fault is present. This trajectory of the  $\text{CO}_2$  plume has been observed in the field at Ketzin, Germany (Chen et al., 2014). Thus, the  $\text{CO}_2$  plume may not reach low-permeable faults, which could be the only potential migration path for  $\text{CO}_2$  if a fault was reactivated. Still, this possibility is remote, because clay-rich materials, like a fault that crosses a clay-rich rock, tend to maintain low-permeability and high entry pressure despite shear slip accumulation (Laurich et al., 2014). In the eventual case of the  $\text{CO}_2$  plume reaching the fault, the pore pressure in the fault will be almost equal to  $\text{CO}_2$  pressure. Thus, the  $\text{CO}_2$ -rich phase will not easily flow through extensional faults due to their multi-phase flow properties (Fisher and Knipe, 2001).

The fault considered in this study corresponds to a conduit-barrier fault in the section crossing the reservoir (Caine et al.,

1996). However, the conduit does not have continuity across the confining layers due to the fault heterogeneity (Rinaldi et al., 2014). Though the type of fault that we model is typical for sedimentary formations with alternating layers of clastic and clay-rich materials (Egholm et al., 2008), different lithology and geologic histories can lead to different fault structures (Faulkner et al., 2010). For example, the presence of a very stiff caprock, with low clay content and thus being brittle, may lead to permeability enhancement if fault reactivation occurs. But even with the fault structure considered here, differences in the degree of calcite cementation of the damage zone (Alikarami et al., 2013), or dissymmetry in the internal structure of the damage zone (Rohmer, 2014; Rohmer et al., 2014), may produce different geomechanical responses of the fault. Thus, subsurface uncertainty may play a relevant role in fault stability assessment (Pereira et al., 2014; Wei et al., 2015).

In this study, we assume brittle behavior of rock, i.e. elastic deformation up to failure. This is the least conservative situation, because for storage formation, fault, and caprock representatives, quasi-brittle or even ductile behavior is common at typical geologic carbon storage stress states (e.g. Popp and Salzer, 2007; Makhnenko and Labuz, 2015). This ductile behavior implies rock yielding before failure. Thus, between the onset of yield and the failure of the rock, a transition zone in which both elastic and plastic strains occur may allow accumulating large strain without inducing large stresses. Additionally, the dilatancy of the storage formation (Makhnenko and Labuz, 2015), the confining layers (e.g. Popp and Salzer, 2007), or the fault-forming material (Parry and Bruhn, 1990) would lead to pore pressure reduction. Furthermore, dilatant hardening may arrest the rupture, especially for the case of confining layers, where undrained deformation occurs.

Since we are assuming only elastic deformation, the mobilized friction angle reaches values above the actual friction angle typical of the rock types considered in the model, i.e.  $30^\circ$ . These high mobilized friction angles are due to the fact that no pressure management is carried out during the simulations. However, it permits identifying which is the most critical zone around the fault. The highest mobilized friction angle takes place in the pressurized region of the storage formation, around 0.5 m away from the damage zone. This observation may be correlated with the fact that the damage zone of faults tends to increase as shear slip events accumulate (Billi et al., 2003). If the most critical zone is located outside the fault, the rock there may fail and widen the thickness of the damage zone. However, this is not a straightforward process, since the friction angle of intact rock is higher than that of failed rock and therefore, the fault is more likely to fail earlier than the intact rock. Furthermore, once failure occurs, stresses are released and the mobilized friction angle is reduced around the fault. Thus, rock around the fault would not reach failure conditions despite the large values of mobilized friction angles observed on both sides of the fault (see Fig. 5).

The shear stress changes that occur in the fault have, in general, the opposite sign to the shear stress acting on the fault plane due to the regional normal faulting stress regime, especially when injecting in the hanging wall (Fig. 11e). This orientation of the shear stress increments is due to the fact that  $\text{CO}_2$  injection causes the expansion of the storage formation. If  $\text{CO}_2$  is injected in the hanging wall, the expansion pushes the upper half of the hanging wall upwards (contrary to the regional stress state) and the lower part downwards (in the same direction as the regional stress state) (Fig. 4e). On the other hand, if  $\text{CO}_2$  is injected in the foot wall, the expansion pushes the upper half of the foot wall upwards (in the same direction as the regional stress state) and the lower part downwards (contrary to the regional stress state) (Fig. 9e). However, if shear failure conditions are reached in the fault, inelastic strain will bring the hanging wall downwards and the foot wall

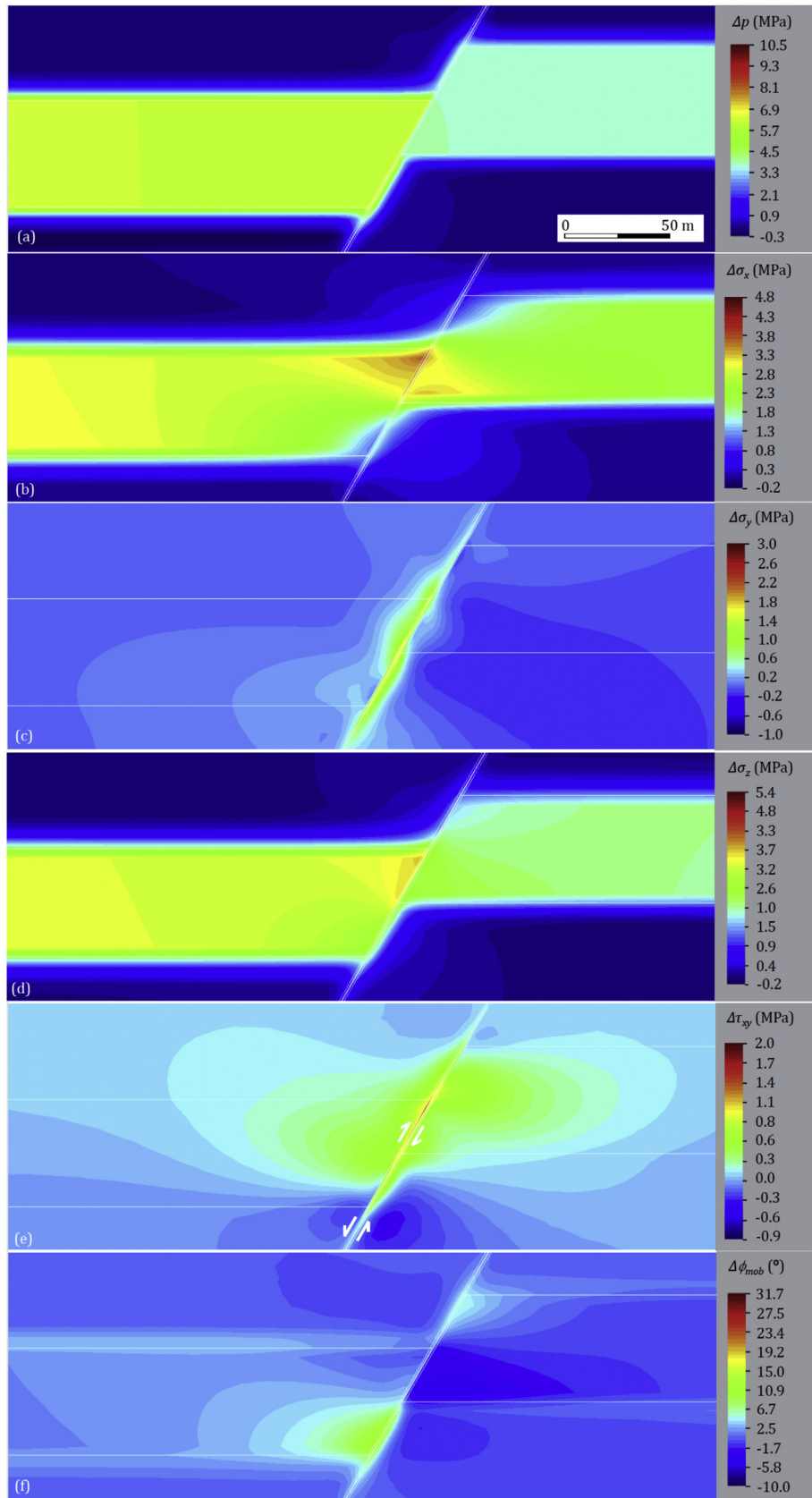


**Fig. 11.** Distribution of changes in (a) fluid pressure, (b) minimum horizontal total stress (in-plane), (c) vertical total stress, (d) maximum horizontal total stress (out-of-plane), (e) shear stress, and (f) mobilized friction angle after one year of injecting CO<sub>2</sub> in the hanging wall when the permeability of the fault core is of 10<sup>-17</sup> m<sup>2</sup> (two orders of magnitude more permeable than that of the base case).

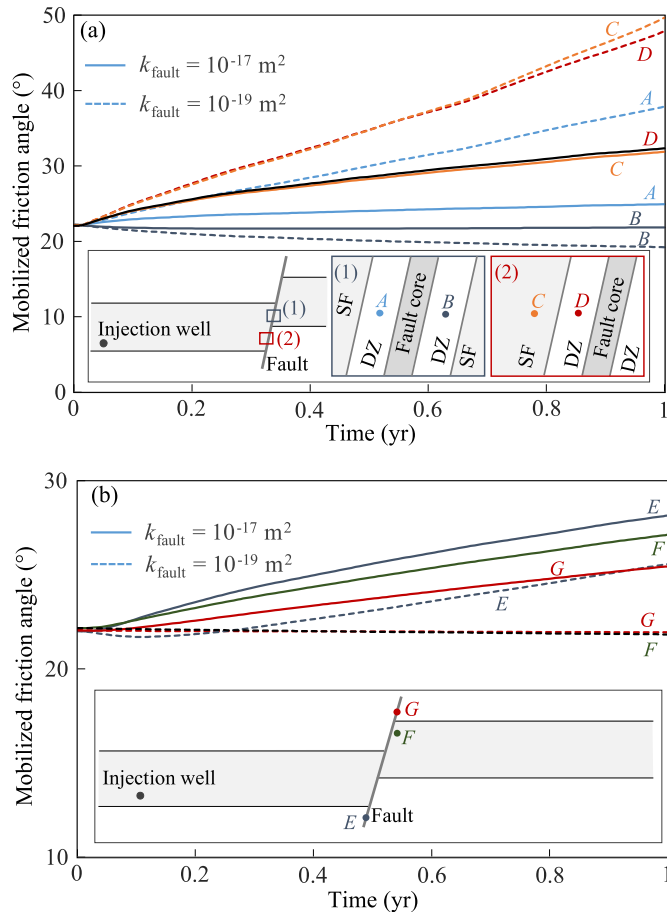


**Fig. 12.** Evolution of the mobilized friction angle at several points when injecting  $\text{CO}_2$  in the hanging wall for a fault core permeability of  $10^{-17} \text{ m}^2$  (the results for a fault core permeability of  $10^{-19} \text{ m}^2$ , in dashed lines, are shown for comparison) (a) in and close to the fault in the pressurized part of the storage formation and (b) below and above the storage formation and in the upper portion of the storage formation that is not pressurized.

upwards, because the shear stress acting on the fault due to the regional stress state is much larger than the shear stress changes induced by  $\text{CO}_2$  injection.

Fault stability is mainly controlled, in our model, by the offset of the fault. The difference in the stiffness between the storage formation and the caprock and base rock, of one order of magnitude, leads to non-homogeneous total stress changes around the fault, which significantly affect its stability. In the case of a larger fault offset when only base rock or caprock is present on the other side of the fault, the storage formation around the fault would undergo a smaller increase in the horizontal total stress in the direction perpendicular to the fault. This may lead to unstable conditions due to the high deviatoric stress and reduced normal effective stress, i.e. the Mohr circle maintains its size and is displaced towards the failure envelope (Orlic and Wassing, 2013). In contrast, in the case of a small fault offset, which would imply having the storage formation on both sides of the fault, the horizontal total stress in the direction perpendicular to the fault would increase significantly around the fault due to the high stiffness of the storage formation. As a result, the size of the Mohr circle would become smaller, which would help to maintain fault stability (Gheibi et al., 2016). The changes in the vertical total stress are more difficult to be predicted without actually simulating these scenarios, but in principle, the stiffer the rock on the other side of the fault, the higher the increase in the total vertical stress. Nevertheless, vertical stress changes are

smaller than horizontal stress changes, so they have less effect on fault stability.

Fault stability is also controlled by other factors, such as the initial stress state, fault dip and geometry of the storage formation. We have considered an initial stress state typical of sedimentary formations, which are usually not critically stressed and thus, a certain overpressure can be induced without reaching failure conditions (Vilarrasa and Carrera, 2015). However, initial stress states that are close to failure conditions, like that occurring in the crystalline basement, lead to fault reactivation for small overpressures (Figueiredo et al., 2015) and have the potential to induce larger earthquakes for a given injection rate (Cappa and Rutqvist, 2011a). We have considered a critically oriented fault in a normal faulting stress regime for a fault with a typical friction angle of  $30^\circ$ . Even though fault reactivation is possible in faults that are not critically oriented, a fault dip different from the considered one would have required a larger overpressure to reach shear failure conditions. As for the geometry of the storage formation, a thicker storage formation would lead to a higher transmissivity. Thus, the effect would be similar to that of a higher permeability or a lower injection rate. In all these cases, pressure build-up would have been slower, so failure conditions would have been reached at a later injection time.

For the considered injection mass flow rate, shear failure conditions are reached within the first year of  $\text{CO}_2$  injection for the cases with a fault core permeability of  $10^{-19} \text{ m}^2$ . However, for the case of a fault core permeability of  $10^{-17} \text{ m}^2$ , the fault may remain stable, at least during the first year of injection. Thus, one could imagine the possibility that if a reactivation of a low-permeable fault occurs and leads to an increase in fault permeability by several orders of magnitude, the fault may remain stable afterwards even though the same injection rate is maintained. Nevertheless, fault permeability may not experience a significant increase after its reactivation in clay-rich formations (Laurich et al., 2014). In fact, we have experimentally observed that even if failure of clay-rich caprock and base rock representative (shale) or fault core material (remolded shale) occurs, the overall change in void ratio that contributes to the flow does not exceed 2% (see also Popp and Salzer, 2007). This increase in void ratio provides less than an order of magnitude increase in fault permeability, which, as shown in Section 3.3, leads to a smaller effect on its stability. Still, the safety of the storage procedure may be compromised if fluid pressure exceeds the maximum sustainable injection pressure. Thus, the overall safety of geologic storage projects, in terms of the possibility of  $\text{CO}_2$  leakage through the fault or the caprock, is subjected to proper monitoring and pressure management.

## 5. Conclusions

Injection of  $\text{CO}_2$  either in the hanging wall or in the foot wall has a very similar effect on fault stability changes. Simulation results show that the stress changes that occur around the fault as a result of  $\text{CO}_2$  injection cause a significant reduction in fault stability. However, both the storage formation and the caprock remain stable at relatively short distances from the fault. Despite the large pressure build-up that takes place between the injection well and the fault, caprock stability around the injection well is not compromised and thus, its sealing capacity is maintained, so  $\text{CO}_2$  leakage will not occur. The most critical zone occurs around 0.5 m outside the fault, which may result in the widening of the damage zone. We find that the permeability of the fault core has a significant influence on fault stability. The lower the fault core permeability is, the higher the induced overpressure and stress changes are. Thus, less permeable faults lead to less stable situations. Overall, pressure management should be performed to minimize the risk of inducing felt seismic events.

## Conflict of interest

The authors wish to confirm that there are no known conflicts of interest associated with this publication and there has been no significant financial support for this work that could have influenced its outcome.

## Acknowledgements

The first author acknowledges the support from the “EPFL Fellows” fellowship program co-funded by Marie Curie, FP7 (Grant No. 291771) and partial support from the “TRUST” project of the European Community’s Seventh Framework Programme FP7/2007–2013 (Grant No. 309607) and the “FracRisk” project of the European Community’s Horizon 2020 Framework Programme H2020-EU.3.3.2.3 (Grant No. 640979). Activities of the second author are sponsored by SCCER-SoE (Switzerland) (Grant No. KTI.2013.288) and Swiss Federal Office of Energy (SFOE) project CAPROCK (Grant No. 810008154). This publication has also been produced with partial support from the BIGCCS Centre (for the third author), performed under the Norwegian research program Centers for Environment-friendly Energy Research (FME). The third author acknowledges the following partners for their contributions: Gassco, Shell, Statoil, TOTAL, ENGIE, and the Research Council of Norway (193816/S60).

## References

- Alikarami R, Torabi A, Kolyukhin D, Skurtveit E. Geostatistical relationships between mechanical and petrophysical properties of deformed sandstone. *International Journal of Rock Mechanics and Mining Sciences* 2013;63:27–38.
- Bear J. *Dynamics of fluids in porous media*. New York: Elsevier; 1972.
- Bennion B, Bachu S. Drainage and imbibition relative permeability relationships for supercritical CO<sub>2</sub>/brine and H<sub>2</sub>S/brine systems in intergranular sandstone, carbonate, shale, and anhydrite rocks. *SPE Reservoir Evaluation & Engineering* 2008;11(3):487–96.
- Billi A, Salvini F, Storti F. The damage zone-fault core transition in carbonate rocks: implications for fault growth, structure and permeability. *Journal of Structural Geology* 2003;25(11):1779–94.
- Birkholzer JT, Zhou Q, Tsang CF. Large-scale impact of CO<sub>2</sub> storage in deep saline aquifers: a sensitivity study on pressure response in stratified systems. *International Journal of Greenhouse Gas Control* 2009;3(2):181–94.
- Birkholzer JT, Oldenburg CM, Zhou Q. CO<sub>2</sub> migration and pressure evolution in deep saline aquifers. *International Journal of Greenhouse Gas Control* 2015;40:203–20.
- Byerlee JD. *Friction of rocks*. Pure and Applied Geophysics 1978;116(4):615–26.
- Caine JS, Evans JP, Forster CB. Fault zone architecture and permeability structure. *Geology* 1996;24(11):1025–8.
- Cappa F, Rutqvist J. Impact of CO<sub>2</sub> geological sequestration on the nucleation of earthquakes. *Geophysical Research Letters* 2011a;38(17). <http://dx.doi.org/10.1029/2011GL048487>.
- Cappa F, Rutqvist J. Modeling of coupled deformation and permeability evolution during fault reactivation induced by deep underground injection of CO<sub>2</sub>. *International Journal of Greenhouse Gas Control* 2011b;5(2):336–46.
- Cappa F, Rutqvist J. Seismic rupture and ground accelerations induced by CO<sub>2</sub> injection in the shallow crust. *Geophysical Journal International* 2012;190(3):1784–9.
- Castelletto N, Gambolati G, Teatini P. Geological CO<sub>2</sub> sequestration in multi-compartment reservoirs: geomechanical challenges. *Journal of Geophysical Research: Solid Earth* 2013;118(5):2417–28.
- Cesca S, Grigoli F, Heimann S, González Á, Buforn E, Maghsoudi S, Blanch E, Dahm T. The 2013 September–October seismic sequence offshore Spain: a case of seismicity triggered by gas injection? *Geophysical Journal International* 2014;198(2):941–53.
- Chen F, Wiese B, Zhou Q, Kowalsky MB, Norden B, Kempka T, Birkholzer JT. Numerical modeling of the pumping tests at the Ketzin pilot site for CO<sub>2</sub> injection: model calibration and heterogeneity effects. *International Journal of Greenhouse Gas Control* 2014;22:200–12.
- Detournay E, Cheng AHD. Fundamentals of poroelasticity. In: *Comprehensive rock engineering: principles, practice and projects. Analysis and design method*. New York: Pergamon Press; 1993. p. 113–71.
- Egholm DL, Clausen OR, Sandiford M, Kristensen MB, Korstgård JA. The mechanics of clay smearing along faults. *Geology* 2008;36(10):787–90.
- Ellsworth WL. Injection-induced earthquakes. *Science* 2013;341(6142). <http://dx.doi.org/10.1126/science.1225942>.
- Faulkner DR, Jackson CAL, Lunn RJ, Schlische RW, Shipton ZK, Wibberley CAJ, Withjack MO. A review of recent developments concerning the structure, mechanics and fluid flow properties of fault zones. *Journal of Structural Geology* 2010;32(11):1557–75.
- Figueiredo B, Tsang CF, Rutqvist J, Bensabat J, Niemi A. Coupled hydro-mechanical processes and fault reactivation induced by CO<sub>2</sub> injection in a three-layer storage formation. *International Journal of Greenhouse Gas Control* 2015;39:432–48.
- Fisher QJ, Knipe RJ. The permeability of faults within siliciclastic petroleum reservoirs of the North Sea and Norwegian Continental Shelf. *Marine and Petroleum Geology* 2001;18(10):1063–81.
- Fuss S, Canadell JG, Peters GP, Tavoni M, Andrew RM, Ciais P, Jackson RB, Jones CD, Kraxner F, Nakicenovic N, Le Quééré C, Raupach MR, Sharifi A, Smith P, Yamagata Y. Betting on negative emissions. *Nature Climate Change* 2014;4(10):850–3.
- Gheibi S, Holt R, Vilarrasa V. Stress path evolution during fluid injection into geological formations. In: *The 50th US Rock Mechanics/Geomechanics Symposium*, Houston, USA. American Rock Mechanics Association; 2016. Paper 16–614.
- Hansen O, Gilding D, Nazarian B, Osdal B, Ringrose P, Kristoffersen JB, Eiken O, Hansen H. Snøhvit: the history of injecting and storing 1 Mt CO<sub>2</sub> in the Fluvial Tubåen Fm. *Energy Procedia* 2013;37:3565–73.
- Horton S. Disposal of hydrofracking waste fluid by injection into subsurface aquifers triggers earthquake swarm in central Arkansas with potential for damaging earthquake. *Seismological Research Letters* 2012;83(2):250–60.
- Hsieh PA. Deformation-induced changes in hydraulic head during ground-water withdrawal. *Ground Water* 1996;34(6):1082–9.
- Håring MO, Schanz U, Ladner F, Dyer BC. Characterisation of the Basel 1 enhanced geothermal system. *Geothermics* 2008;37(5):469–95.
- International Energy Agency (IEA). *Energy technology perspectives. Scenarios & strategies to 2050*. Executive summary. IEA; 2010.
- Laurich B, Urai JL, Desbois G, Vollmer C, Nussbaum C. Microstructural evolution of an incipient fault zone in Opalinus Clay: insights from an optical and electron microscopic study of ion-beam polished samples from the Main Fault in the Mt-Terri Underground Research Laboratory. *Journal of Structural Geology* 2014;67:107–28.
- Makhnenko RY, Labuz JF. Dilatant hardening of fluid-saturated sandstone. *Journal of Geophysical Research: Solid Earth* 2015;120(2):909–22.
- Makhnenko RY, Labuz JF. Elastic and inelastic deformation of fluid-saturated rock. *Philosophical Transactions of the Royal Society A: Mathematical, Physical & Engineering Sciences* 2016. <http://dx.doi.org/10.1098/rsta.2015.0422>.
- Mazzoldi A, Rinaldi AP, Borgia A, Rutqvist J. Induced seismicity within geological carbon sequestration projects: maximum earthquake magnitude and leakage potential from undetected faults. *International Journal of Greenhouse Gas Control* 2012;10:434–42.
- Oldenburg CM. The risk of induced seismicity: is cap-rock integrity on shaky ground? *Greenhouse Gases: Science and Technology* 2012;2(4):217–8.
- Olivella S, Carrera J, Gens A, Alonso EE. Non-isothermal multiphase flow of brine and gas through saline media. *Transport in Porous Media* 1994;15(3):271–93.
- Olivella S, Gens A, Carrera J, Alonso EE. Numerical formulation for a simulator (CODE\_BRIGHT) for the coupled analysis of saline media. *Engineering Computations* 1996;13(7):87–112.
- Orlic B, Wassing BBT. A study of stress change and fault slip in producing gas reservoirs overlain by elastic and viscoelastic caprocks. *Rock Mechanics and Rock Engineering* 2013;46(3):421–35.
- Pan PZ, Rutqvist J, Feng XT, Yan F. Modeling of caprock discontinuous fracturing during CO<sub>2</sub> injection into a deep brine aquifer. *International Journal of Greenhouse Gas Control* 2013;19:559–75.
- Pan PZ, Rutqvist J, Feng XT, Yan F. An approach for modeling rock discontinuous mechanical behavior under multiphase fluid flow conditions. *Rock Mechanics and Rock Engineering* 2014;47(2):589–603.
- Parry WT, Bruhn RL. Fluid pressure transients on seismogenic normal fault. *Tectonophysics* 1990;179(3–4):335–44.
- Pereira LC, Guimarães LJM, Horowitz B, Sánchez M. Coupled hydro-mechanical fault reactivation analysis incorporating evidence theory for uncertainty quantification. *Computers and Geotechnics* 2014;56:202–15.
- Popp T, Salzer K. Anisotropy of seismic and mechanical properties of Opalinus Clay during triaxial deformation in a multi-anvil apparatus. *Physics and Chemistry of the Earth, Parts A/B/C* 2007;32(8–14):879–88.
- Rinaldi AP, Jeanne P, Rutqvist J, Cappa F, Guglielmi Y. Effects of fault-zone architecture on earthquake magnitude and gas leakage related to CO<sub>2</sub> injection in a multi-layered sedimentary system. *Greenhouse Gases: Science and Technology* 2014;4(1):99–120.
- Rinaldi AP, Vilarrasa V, Rutqvist J, Cappa F. Fault reactivation during CO<sub>2</sub> sequestration: effects of well orientation on seismicity and leakage. *Greenhouse Gases: Science and Technology* 2015;5(5):645–56.
- Rohmer J. Induced seismicity of a normal blind undetected reservoir-bounding fault influenced by dissymmetric fractured damage zones. *Geophysical Journal International* 2014;197(1):636–41.
- Rohmer J, Allanic C, Bourguin B, Sulem J, Suhett-Helmer G, Ghabezloo S, Pouya A, Renard F, Beucher H, Mehl C, Siavelis M, Tardieu N. Improving our knowledge on the hydro-chemo-mechanical behaviour of fault zones in the context of CO<sub>2</sub> geological storage. *Energy Procedia* 2014;63:3371–8.
- Rutqvist J. The geomechanics of CO<sub>2</sub> storage in deep sedimentary formations. *Geotechnical and Geological Engineering* 2012;30(3):525–51.

- Streit JE, Hillis RR. Estimating fault stability and sustainable fluid pressures for underground storage of CO<sub>2</sub> in porous rock. *Energy* 2004;29(9–10):1445–56.
- Szulczewski ML, MacMinn CW, Herzog HJ, Juanes R. Lifetime of carbon capture and storage as a climate-change mitigation technology. *Proceedings of the National Academy of Sciences of the United States of America* 2012;109(14):5185–9.
- Verdon JP. Significance for secure CO<sub>2</sub> storage of earthquakes induced by fluid injection. *Environmental Research Letters* 2014;9(6):064022.
- Vidal-Gilbert S, Tenthorey E, Dewhurst D, Ennis-King J, Van Ruth P, Hillis R. Geomechanical analysis of the Naylor Field, Otway Basin, Australia: implications for CO<sub>2</sub> injection and storage. *International Journal of Greenhouse Gas Control* 2010;4(5):827–39.
- Vilarrasa V, Carrera J, Olivella S. Hydromechanical characterization of CO<sub>2</sub> injection sites. *International Journal of Greenhouse Gas Control* 2013a;19:665–77.
- Vilarrasa V, Silva O, Carrera J, Olivella S. Liquid CO<sub>2</sub> injection for geological storage in deep saline aquifers. *International Journal of Greenhouse Gas Control* 2013b;14:84–96.
- Vilarrasa V, Olivella S, Carrera J, Rutqvist J. Long term impacts of cold CO<sub>2</sub> injection on the caprock integrity. *International Journal of Greenhouse Gas Control* 2014;24:1–13.
- Vilarrasa V, Carrera J. Geologic carbon storage is unlikely to trigger large earthquakes and reactivate faults through which CO<sub>2</sub> could leak. *Proceedings of the National Academy of Sciences of the United States of America* 2015;112(19):5938–43.
- Wei XC, Li Q, Li XY, Sun YK, Liu XH. Uncertainty analysis of impact indicators for the integrity of combined caprock during CO<sub>2</sub> geosequestration. *Engineering Geology* 2015;196:37–46.
- Zhou Q, Birkholzer JT. On scale and magnitude of pressure build-up induced by large-scale geologic storage of CO<sub>2</sub>. *Greenhouse Gases: Science and Technology* 2011;1(1):11–20.

- Zoback MD, Gorelick SM. Earthquake triggering and large-scale geologic storage of carbon dioxide. *Proceedings of the National Academy of Sciences of the United States of America* 2012;109(26):10164–8.



**Victor Vilarrasa** obtained M.S. and Ph.D. degrees from the Technical University of Catalonia (UPC), Barcelona, Spain. He was a postdoctoral fellow at the Earth and Environmental Sciences Area at the Lawrence Berkeley National Laboratory (LBNL), Berkeley, USA and was awarded with an 'EPFL Fellows' Fellowship co-funded by Marie Curie at the École Polytechnique Fédérale de Lausanne, Switzerland. He is now staff scientist at the Institute of Environmental Assessment and Water Research, Spanish National Research Council (IDAEA-CSIC). His research, developed in several European and US research projects, deals with dimensional analysis and modeling of coupled thermo-hydro-mechanical-chemical (THMC) processes related to geo-energy and geo-engineering applications. He applies

his research to several geo-energy and geo-engineering applications, such as CO<sub>2</sub> geologic storage, geologic nuclear waste disposal and enhanced geothermal systems. He has given several invited talks at conferences and seminars, including universities such as Stanford University, Swiss Federal Institute of Technology Zurich (ETHZ) and the Royal Institute of Technology (KTH), and research institutes such as the US Geologic Survey (USGS) and LBNL. He serves as a reviewer in many geoscience journals. Up to now he has received the Special Doctoral Award of the UPC, the Alfons Bayó Award to Young Researchers awarded by the International Association of Hydrogeologists (IAH) – Spanish Group, and the MIT Technology Review Award to Innovators Under 35.